Electron-diffraction study of rubidium-intercalated graphite

Richard K. Mittleman
The Enrico Fermi Institute, The University of Chicago, 5640 South Ellis Avenue, Chicago, Illinois 60637
(Received 2 April 1987)

Using an analytical scanning transmission electron microscope we monitored the in-plane structure of rubidium-intercalated graphite as it underwent the deintercalation process. Starting with a saturated, stage-1 sample and using a temperature-controlled sample stage to control the desorption process, we allowed the graphite to deintercalate over a period of many days. This created a series of unannealed structures of progressively higher stage number. The experiment encompassed a regime in which the dominant factor in determining the intercalant in-plane distribution changed from host-intercalant to intercalant-intercalant interactions. High-resolution electron diffraction techniques were used to follow the in-plane superlattice structure of the intercalant. Ordered commensurate superlattices were observed which were stable over the entire temperature range observed (79–300 K) . In addition, an amorphous phase was observed which underwent a phase transition to an incommensurate square array. Both commensurate and incommensurate transition structures were observed during the transition period. The incommensurate structure was not affected by temperature and does not match the general lattice parameters for incommensurate lattices which have been previously reported in the alkali-metal-intercalated graphite compounds.

INTRODUCTION

The physics of competing periodicities has been a topic of great interest recently. This subject has applications in a number of different physical situations including the junctions of dissimilar materials, surface-adsorbed gases, and intercalated materials. Intercalated materials are a particularly good arena for these studies since the experimenter has the ability to control many of the system parameters by adjusting the amount of intercalant within the host material. It has been observed that the host-intercalant and host-adsorbate interaction strength is a function of the guest concentration with commensurate-incommensurate phase transitions taking place with density changes. Another interesting factor in adjusting the guest density in intercalated systems is that a smooth transition from a three-dimensional to a quasi-two-dimensional interaction regime takes place.[1–4]

Although the phenomena of intercalation has been known for 3000 years[5] it has only become a subject of scientific research fairly recently when Schaffäutl reported the synthesis of graphite intercalation compound in 1841.[6] With the advent of x-ray diffraction techniques in the 1930's the staging properties of intercalated materials were the first to be widely studied.[7,8] From these and other sources such as electron microscopy studies[9] and neutron diffraction[10] it has been found that the intercalant is arranged so as to form layered structures with a constant number of layers of the host between each layer of intercalant. The number of host layers is called the stage number of the composite material. Graphite intercalant compounds (GIC's) of well-defined stage number have been prepared with stage numbers from 1 to 11. These and other studies have shown a sharp phase transition between stages as the amount of intercalated material changes. This observation led to the Daumas-Hérold model, which describes the distribution of intercalant within the graphite.[11] In this model the intercalant is grouped into islands ranging in size from 100 Å to a few micrometers depending on the material. There are islands of intercalant between every pair of graphite layers with each individual island maintaining the proper c-axis spacing relative to other islands.

The alkali-metal–graphite intercalation compounds (AM-GIC's) are among the most widely studied intercalation compounds for a number of reasons. One of the original motivations was that they are relatively easy to produce, in particular the synthesis of pure stage compounds is a straightforward process.[3] With the proper annealing procedures some of these compounds can be made with long-range stacking (three-dimensional) orders.[10] Four of the members of the alkali family easily intercalate into graphite (Li,K,Rb,Cs) and provide an arena for studying the effects of varied ionization potential, ionic radii, etc., on the properties of the final compound. The AM-GIC's are highly ionizing donor compounds, which highly modify the properties of the host material. The high electron mobility of the graphite layers can lead to properties in the compound material unlike those of either of the original species. One interesting example is the superconducting phenomena in the first-stage K-GLC's below 1.0 K.[12,13] The higher-stage AM-GIC's ($n \geq 2$) have come under scrutiny lately due to the in-plane phase changes at constant stage number which they have been reported to undergo as a function of temperature or pressure.[14] In the course of these examinations an incommensurate in-plane triangular lattice has been reported at low temperatures for the stage-2 heavy AM-GIC's[15] (K, Rb, or Cs).

In 1926 Fredenhagen[16] proposed that the intercalant-to-carbon ratio in GIC's should be an integer. Following this suggestion and on the basis of their work of measuring the mass of alkali metal absorbed in various-stage Rb- and K-GIC's Rüdorff and Schulze[17] proposed

a stoichiometry of C_8M for the first-stage compound and $C_{12n}M$ (where $n \geq 2$ is the stage number) for the higher stages. In the same paper they suggested as in-plane lattice structure to account for the 8:1 ratio. Their suggestion for the first-stage structure was a $p(2\times2)R0°$.[18] In 1967 Parry and Nixon confirmed this proposal using x-ray diffraction of stage-1 K- and Rb-GIC's.[19] They also found that when annealed these materials produce structures with long-range regular stacking sequences and three-dimensional ordering. This observation has been confirmed many times, particularly when Kambe *et al.*,[20] using electron diffraction on Rb samples, reported a reversible stacking-disorder transition at 300 K. There is no commensurate triangular superlattice which matches the stoichiometry for the higher-stage compounds and Parry and Nixon proposed a honeycombed structure, $h(\sqrt{12}\times\sqrt{12})R30°$, to fit this stoichiometry. Although this structure seems to be a natural transition from the (2×2), first-stage material, it has not been observed. Clarke *et al.*[15] have reported measurements confirming the $C_{12n}M$ stoichiometry in stage-2 and -3 Cs-GIC's, however, many have questioned the validity of any particular ratio. Using x-ray scattering techniques Caswell[21] reported a continuous change in the equilibrium intercalant concentration of a stage-1 Cs-GIC from C_8Cs to $C_{n>10}Cs$.

The reported structural behavior of these materials has varied widely, apparently depending on the probing technique and sample preparation method employed. A number of phase transitions as a function of temperature have been reported[20] for the stage-2 Rb-intercalated graphite compound. The most commonly observed transitions are seen below room temperature in the neighborhood of 105 and 165 K,[22] although other researchers have found similar transitions at different temperatures.[23] The behavior from room temperature to the first transition temperature has been reported to be a disordered in-plane distribution of intercalant atoms.[24,25] At the higher transition temperature an order-disorder transition to an incommensurate triangular lattice takes place. This lattice changes size and rotation angle until the lower transition is reached where three-dimensional ordering appears and the lattice freezes in. There have been reports of three-dimensional ordering in the intermediate temperature region.[15,26] Due to a bias towards commensurate structures earlier work had interpreted this structure to be a combination of commensurate lattices. Mori *et al.* first suggested an empirical formula for the relationship between the incommensurate lattice and the rotation angle for all the heavy AM-GIC's.[27]

$$\cos(30°-\theta)=\frac{1+2z^2}{2\sqrt{3}z} ,$$

$$z=|\mathbf{Q}_1|/|\mathbf{G}_1| ,$$

where $\mathbf{Q}_1$ is the first-order intercalant inverse lattice vector (Å^{-1}), $\mathbf{G}_1$ is the first-order graphite inverse lattice vector (2.95 Å^{-1}), and θ is the rotation of the alkali inverse lattice from $\mathbf{G}_1$. There have been two separate interpretations which seem to fit this data, and produce diffraction patterns similar to those observed. Both incorporate the results of Caswell *et al.*[28] who used extended x-ray-absorbtion fine-structure techniques on K-GIC's to show that the intercalant ions lie in the centers of the graphite hexagonal lattice sites. Other experiments on high-stage Cs-GIC's have found that the cesium ions form a "floating liquid" in which the cesium atoms are positionally uncorrelated with the graphite host. Clarke *et al.*[29] proposed a discommensurate domain model to explain the incommensurate x-ray diffraction patterns. This idea was first suggested by Frank and ven der Merwe over 30 years ago in connection with gas layers adsorbed onto a graphite substrate.[30] In this model a weakly incommensurate layer of intercalant is formed in a domain structure in which the order is locally commensurate [$p(\sqrt{7}\times\sqrt{7})R19.1°$ for the AM-GIC]. This order is modulated by a periodic array of misfit dislocations, or by the domain walls, where the discommensurations take place. The second is a model suggested by DiCenzo[31] which is conceptually somewhat simpler. In this model the intercalant positions are generated by laying a triangular lattice over the graphite lattice and assuming that the graphite layer will have the effect of moving the intercalant atoms into the nearest "hole" in the graphite honeycombed layer.

METHODS

The sample was prepared from highly oriented pyrolytic graphite (HOPG) samples which had been thinned prior to the intercalation process.[32] D. M. Hwang performed the intercalation process using the standard two-temperature-zone method.[3] HOPG is an artificially produced graphite material which is well ordered in the *c*-axis direction with domains on the scale of tens of micrometers in the planar direction. These domains have a mosaic spread of approximately one degree before intercalation which increases to about two degrees after intercalation.[26] The samples were intercalated gradually over many weeks to avoid exfoliation and ensure sample homogeneity.[33] We used a scanning transmission electron microscope at a relatively low voltage of 26 kV to examine the specimens. This technique dictated that our samples had to be particularly thin because the mean-free-path length of electrons in amorphous carbon at this energy is only 400 Å elastic and 260 Å inelastic. The sample was then transferred to our laboratory still sealed in the glass preparation vessel. Rubidium GIC's are unstable in air, so to prevent desorption a specially designed vacuum transfer mechanism[34] was built, which allowed the sample to be inserted into the high-vacuum column with only a brief exposure to 10^{-4} torr of dry nitrogen after it had left its preparation vessel. The sample chamber immediately pumped until it reached 10^{-9} torr and the sample was inserted into the high vacuum column at 10^{-10} torr and lowered to almost liquid-nitrogen temperature (79 K). The entire procedure after opening the preparation vessel took about thirty minutes.

The microscope

A scanning transmission electron microscope (STEM) (Ref. 34) which has been developed at the Enrico Fermi

Institute was used to gather the data. This STEM was developed as an analytical microscope with a high probe current and optimized for analyzing materials. Operating in a medium voltage range of up to 50 kV this machine was designed to combine flexibility with high performance. It is possible to sequentially image a specimen at moderate resolution (15–50 Å), to probe it in diffraction space with 0.1 $Å^{-1}$ resolution (with diffraction-limited spatial resolution) and to take energy-loss spectra of the transmitted beam with energy resolution of better than 0.2 eV. Two separate sets of changeable apertures and three magnetic lenses allow beam angle, current, and resolution to be adjusted to optimize conditions for a given operating mode.

The combination of a magnetic lens above the accelerator and eight interchangable beam-defining apertures allows the specimen probe current to be adjusted with relatively little effect on specimen resolution. High resolution can be maintained at very high beam currents, in excess of 3×10^7 $(e^-/Å^2)$/sec; high enough to record a high signal-to-noise diffraction micrograph of a single layer of graphite in a single scan raster (512×512 pixels in 17 sec).

A second magnetic lens between the beam aperture and the objective lens allows the beam angle to be adjusted to optimize for the particular operating mode in use. This allows diffraction data to be gathered from the convergent beam mode to nearly parallel conditions. In addition, five interchangable spectrometer apertures allow the collection angle to be adjusted to optimize the spectrometer for any running conditions. A liquid-nitrogen dewar is included to allow the examination of samples as a function of temperature (79–300 K). The data was gathered at a beam voltage of 26 kV, which resulted in an electron wavelength of 0.076 Å and an Ewald diffraction sphere radius of 83.68 $Å^{-1}$.

Computer

An interactive computer display system has been developed[34,35] to analyze the microscope data. An IBM 4381-2 mainframe computer is used for computation, and a Metheus Omega 500 display system is used for imaging and interaction. The system was developed to facilitate the measurement process in a flexible manner. Subroutines are written and incorporated in many (computer) languages including APL, which allows analysis to be developed interactively. Our goals were to be able to display the data rapidly, improve the signal-to-noise characteristics of the micrographs, and to analyze the micrographs, specifically diffraction patterns. In order to do this, routines have been written which use a mouse-driven cursor to input one or more unit cells. Extremely complicated unit cells involving hundreds of molecules and many different layers can be simulated. The diffraction pattern is then calculated and displayed on the high-resolution monitor as it would be observed in the microscope. This pattern can then be overlayed onto the original data to compare the fit. In this way many different very complicated but physically reasonable unit cells can be rapidly examined until one is found that fits the data satisfactorily.

EXPERIMENTAL RESULTS

Our intercalated samples, as determined by the transmitted energy-loss spectra, were approximately 400 Å thick. Depending on the stage number this means that we were typically looking at 25–80 layers of intercalant. The path length for elastic scattering of electrons in carbon at 26 kV is 400 Å. Therefore at this specimen thickness the effects of multiple scattering will not be significant for all but the first-stage material.[36] The general absence of pronounced Kikuchi lines and convergent beam electron diffraction (CBED) effects confirms this and allows us to treat the multiple scattering as a minor higher-order correction to the single scattering distribution. Due to the fact that the data is in the form of two-dimensional projections of a three-dimensional sample both the elastic and inelastic images of the samples throughout the experiment were qualitatively indistinguishable. Figures 1(a) and 1(b) are dark-field micrographs using the STEM elastic signal of the sample after a small amount of deintercalation (probably to stage 2) and at 1.4 and 5.6 μm full scale. The bright-island-like structure is due to the nucleation of the intercalated rubidium into Daumas-Hérold domains, which in this specimen have a maximum size of approximately 5000 Å and are typically about 2000 Å across. The dark lines are the boundaries of the domain structures in the HOPG, which are typically many micrometers in size. The diffraction micrographs in this study were generally taken with a spatial resolution of $\simeq$200 Å (within a factor of 2). This puts us well below the size scale of both the host (HOPG) and the intercalant domain sizes and means that a single micrograph should represent the structure of only one island of intercalant. When the electron beam was not positioned on one of the islands the scattering due to intercalant was much weaker.

It is well known that stage-1 Rb-graphite appears gold in color, while higher stages are blue turning progressively slate gray, the color of pristine graphite, as the stage number increases.[3] Despite the many in-plane phase changes which we observed, the color of the bulk sample remained constant. We interpret this to mean that overall there was very little desorption and the bulk of the sample remained as stage 1. The thin areas ($\simeq$500 Å) which were appropriate for examination by transmission electron microscopy were deintercalating at a much higher rate and we associated some of the in-plane phase changes with changes in stage number.

Immediately after the insertion the diffraction pattern had a disordered appearance as shown in Fig. 2. This type of pattern can be produced by assuming that the intercalant formed short "strings" that were well ordered along their length [with a spacing along the string of 5.10 Å$(=\sqrt{3})$], with an irregular spacing perpendicular to this direction. This structure is an $r(2\times\sqrt{3})R0°$ lattice with disorder in the 2 direction. The $2\times\sqrt{3}$ superlattice has the same in-plane density (C_8M) as the more commonly seen 2×2 lattice. While still at 79° K the diffraction pattern was observed to change to that of a 2×2 lattice. Making the assumption that without a change in stage number the in-plane intercalant density will not have increased to reach this structure, then the

average spacing of the strings in the original structure was at most two times the graphite spacing. Using this information we have found a best fit which has an in-plane intercalant density slightly greater than that of the $2\times\sqrt{3}$ lattice.

After being held for a few hours at 79 K the "disordered" structure disappeared, leaving only a 2×2 diffraction pattern as shown in Fig. 3(a). Figure 3(b) shows the in-plane lattice of this structure and Fig. 3(c) is the computer simulation of a diffraction micrograph produced in our microscope from this sample. This matches the commonly seen superlattice for stage-1 AM-GIC's (C_8M). The transition from $2\times\sqrt{3}$ to (2×2) is a very simple one needing only a small change in every other row of intercalant. This might explain how the transition can take place at such a low temperature. Since this structure was reached by desorption and reordering of a saturated structure it does not display the expected long-range stacking order but instead shows a diffraction pattern characteristic of a two-dimensional structure. Figure 3(d) shows a large field (26.1 Å^{-1} across) view of this pattern, the angular distribution is limited by instrumental factors. The intercalant 2×2 diffraction pattern can be seen out to 14.07 Å^{-1}. This structure did not show any changes as a function of temperature throughout the entire temperature range available to us (79–300 K). This behavior is consistent with previous studies on the stage-1 AM-GIC's.[10,20] To speed up the desorption process the specimen was allowed to remain at ambient temperature for the next few days. During this time a $\sqrt{3}\times\sqrt{3}$ phase gradually coalesced until it reached the same intensity as the 2×2 phase. The first appearance of this phase was simultaneous with the appearance of a weak amorphous ring at 1.84 ± 0.1 Å^{-1} spacing which then coalesced into the commensurate $\sqrt{3}\times\sqrt{3}$ superlattice. The development of this lattice is a probable indication of the formation of the next higher stage (2) material. In this phase of the experiment the 2×2 lattice was present in all areas of the specimen while the $\sqrt{3}\times\sqrt{3}$ superlattice varied in intensity from almost as intense as the 2×2 spots to not being present at all. This is probably an indication that the sample was a mixture of stage-1 and stage-2 structures. Figure 4(a) shows an electron diffraction micrograph from an area with only the $\sqrt{3}\times\sqrt{3}$ superlattice present. Figure 4(b) is the unit cell which produces this pattern and Fig. 4(c) is the computer simulation. Figure 5(a) is an electron diffraction micrograph from an area with both $\sqrt{3}\times\sqrt{3}$ and 2×2 superlattices present. The computer simulation of the combination of these two structures is shown in Fig. 5(b).

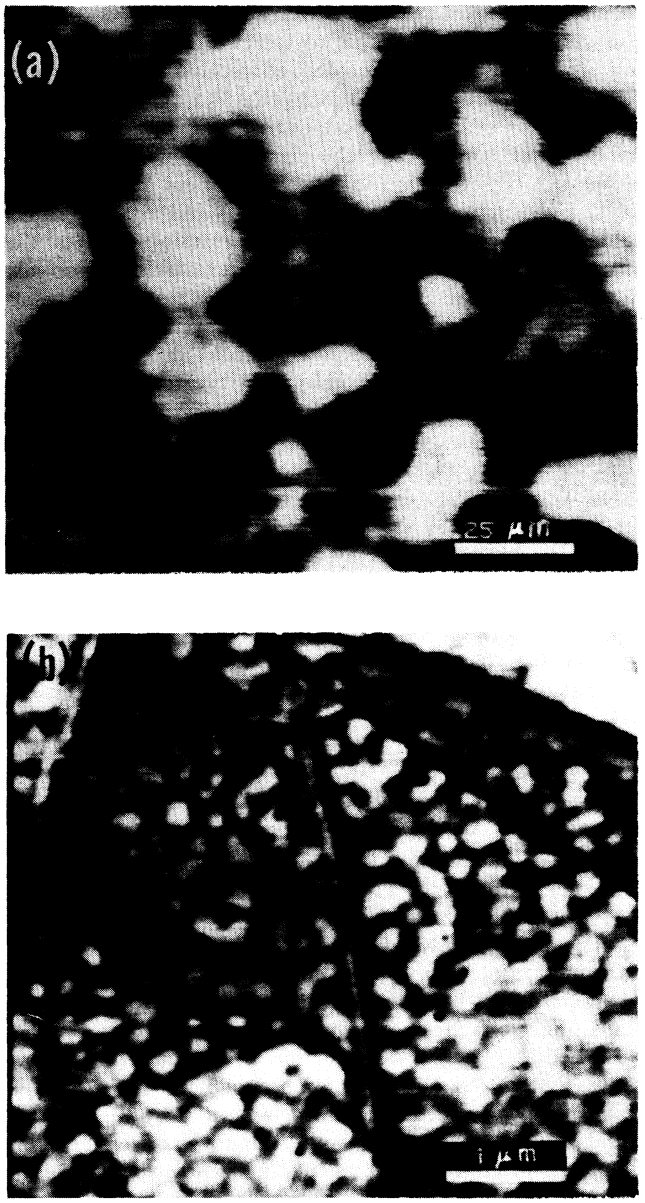

FIG. 1. Dark-field STEM image taken using the elastically scattered electrons. (a) The full scale of the image is 1.4 μm and demonstrates the presence of small islands of rubidium formed within the graphite host. (b) The full scale of the image is 5.6 μm. The dark lines are the boundaries of the HOPG domains.

The high in-plane density of the $\sqrt{3}\times\sqrt{3}$ superlattice, 6.36×10^{-2} atoms/Å^2, makes this lattice somewhat unexpected. It is slightly higher (3%) than the maximum planar density found in a pure rubidium crystal, which is 6.16×10^{-2} atoms/Å^2 in the (111) plane at 20 °C. This is possible because the intercalated rubidium is almost completely ionized[37] with the electrons residing in the neighboring graphite layers. However, if we postulate a second stage structure, the total (three-dimensional) concentration of rubidium is only 56% of that for the pure crystal. The fact that it is always seen in conjunction with the 2×2 phase raises the possibility of a single larger unit cell combined with a long-range c-axis stacking order. For a number of reasons the coexistence of two different unit cells is a more likely explanation, instead of a larger in-plane unit cell. The decrease in diffraction intensity with increasing scattering angle of the two associated structures was not the same. The typical behavior of the 2×2 structure was con-

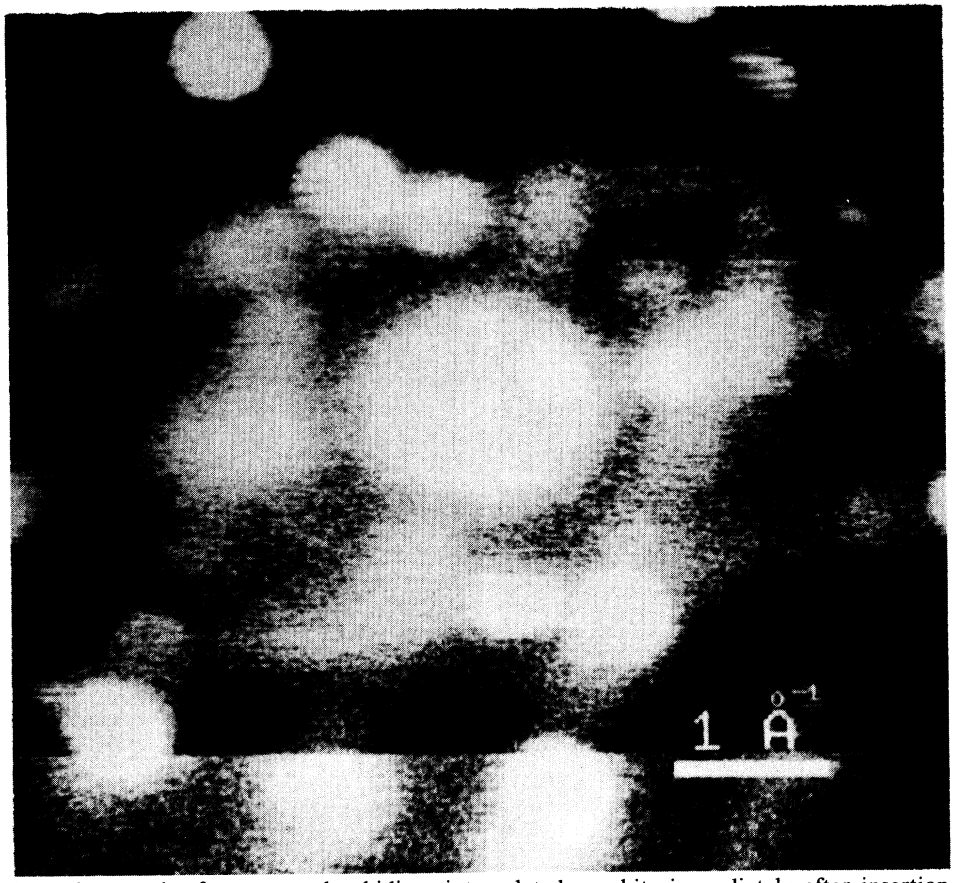

FIG. 2. Diffraction micrograph of a saturated rubidium intercalated graphite immediately after insertion into the analytical STEM. It shows two rotations of a disordered $2\times\sqrt{3}$ superlattice. The graphite diffraction is difficult to see due to the large amount of obscuring rubidium scattering. The micrograph is $\simeq 6$ Å^{-1} across.

sistent with the angular scattering distribution of atomic rubidium [Fig. 3(d)], as would be expected from an infinite two-dimensional structure (much larger than our sampling beam). The angular intensity of the $\sqrt{3}\times\sqrt{3}$ diffraction pattern fell off much more rapidly, suggesting a limitation imposed by short-range ordering. Structures which appear after further desorption exhibit even higher in-plane densities, which eliminates the major objection of a GIC with a higher two-dimensional intercalant density than that of the pure element. The high beam current of our instrument and the very thin specimen (low number of intercalant layers) which we worked with combine so that a misregistration of a few layers will create diffraction in spots that are "forbidden." Stacking faults, or merely end effects, as would be expected in an unannealed sample, will produce incomplete structure factor cancellation which we expect to see as evidence of the larger in-plane unit cell. The low electron voltage (26 kV) at which we operated resulted in an Ewald sphere with radius 83.68 Å^{-1}. The surface of this sphere leaves the first-order plane in inverse space very quickly, and with only a very short c-axis coherence length of a few layers of intercalant the effects of zeros in the structure factor should be noticeable in the diffraction data. The smallest unit cell which contains both of these patterns is $\sqrt{12}\times\sqrt{12}$ and requires a minimum coherence length of seven layers of intercalant to completely duplicate this pattern. The data, however, showed only two-dimensional diffraction patterns, restricting the long-range c-axis ordering to only a few layers. In addition this is not an annealed specimen but one produced by desorption from a saturated specimen at low temperatures, a process which is not expected to produce long-range ordering along the c-axis.

After about a week at ambient temperature a new phase became visible. This new pattern was the $p(\sqrt{12}\times\sqrt{12})R\,30°$ superlattice whose existence had been predicted but had not been commonly seen. An electron diffraction micrograph from this structure is shown in Fig. 6(a). On the basis of the structure of the stage-1 compound and stoichiometric data on high-stage AM-GIC's ($C_{12n}M$, $n\geq 2$),[17] this lattice would seem to be the "natural" result of further desorption. Desorption from a $\sqrt{3}\times\sqrt{3}$ or a 2×2 lattice resulting in a honeycombed lattice $h(\sqrt{12}\times\sqrt{12})$ will account for the diffraction data. Further desorption to a $p(\sqrt{12}\times\sqrt{12})$, without a basis, will also produce satisfactory results. Figure 6(b) shows a $\sqrt{12}\times\sqrt{12}$ unit cell with the appropriate basis location for the "Rüdorff" honeycomb structure labeled with a $+$. In this structure the

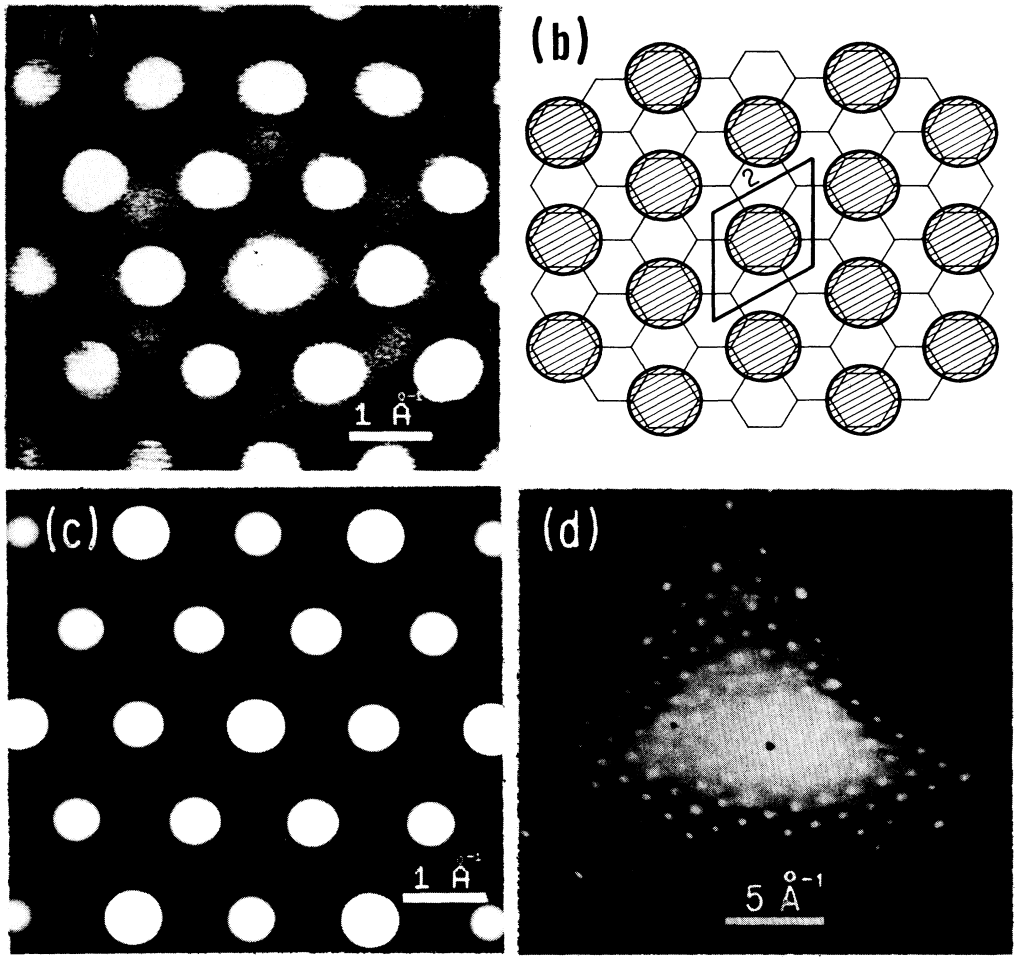

Fig. 3. (a) Diffraction micrograph of the sample while at stage 1. This pattern is characteristic of the $p(2\times2)R0°$ superlattice which is commonly seen in stage-1 heavy AM-GIC's. The micrograph is $\simeq 6$ Å^{-1} across. (b) Sketch of the in-plane unit cell of $p(2\times2)R0°$. The circles represent the locations of the rubidium ions, which are drawn to scale ($r_{Rb^+} = 1.47$ Å). (c) A computer simulation of how an electron diffraction micrograph of $p(2\times2)R0°$ will appear in the analytical STEM. One of the six first-order (100) graphite spots (2.95 Å^{-1}) has been circled in the upper left corner of the micrograph. The scale and orientation are the same as those in (a). (d) Lower-magnification diffraction micrograph of $p(2\times2)R0°$ superlattice. Diffraction from this superlattice is visible beyond 14 Å^{-1}.

diffraction spots associated with a 2×2 lattice were consistently stronger than those associated with a $\sqrt{3}\times\sqrt{3}$ lattice which were in turn more intense than the spots associated only with a $\sqrt{12}\times\sqrt{12}$ lattice. The intensities were roughly in a ratio of 5:3:1 and are most likely indicative of the amount of intercalant in each structure. Figure 6(c) is the computer simulation of this structure using the measured intensity ratios to determine the amount of each structure. This structure was short lived, it was only strongly visible on one day, and can probably be thought of as a transition structure from a 2×2 lattice to a $\sqrt{3}\times\sqrt{3}$ lattice.

The appearance of the next pattern was again accompanied by a strong diffuse ring at 1.84 ± 0.1 Å^{-1} with a second ring visible at 2.9 ± 0.1 Å^{-1}. This phase was characterized by a reversal in the intensities of the 2×2 and the $\sqrt{3}\times\sqrt{3}$ phases. The diffraction spots corresponding to a $\sqrt{3}\times\sqrt{3}$ superlattice increased in intensity with only a slight decrease in the angular falloff of intensity, indicating an increase in the amount of the phase with little increase in the in-plane correlation length. At this time the 2×2 diffraction spots became extremely variable, sometimes being very intense and visible out to high angles while, in nearby positions on the sample (a few thousand angstroms) this pattern was not visible at all. When the 2×2 lattice was not present there was typically a very strong diffuse ring present at 1.84 ± 0.1 Å^{-1} and sometimes weak lines connecting the 2×2 position. There was no sign of any spots in the locations that correspond to only the $\sqrt{12}\times\sqrt{12}$ structure in any of the areas surveyed. The predominance of the $\sqrt{3}\times\sqrt{3}$ lattice was a temporary situation: after a few

days the 2×2 lattice again became the dominant rubidium structure and was apparent out to very high orders. As before, in some locations the $\sqrt{3}\times\sqrt{3}$ lattice was not present while in others it was almost as strong as the 2×2 lattice.

At this point the rubidium lattice underwent a change producing a number of transitory lattices which produced weak diffraction patterns. These structures were in general not well ordered over long ranges and were not the dominant intercalant phase. The 2×2 lattice was still the only long-range intercalant superlattice

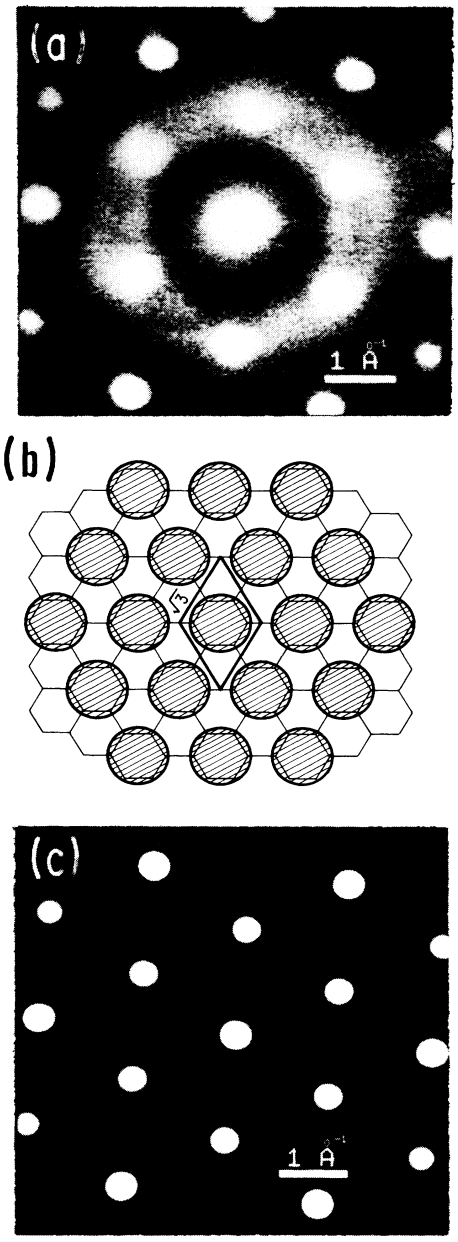

FIG. 4. (a) Diffraction micrograph of the sample while probably at stage number two. This pattern is characteristic of a $p(\sqrt{3}\times\sqrt{3})R30°$ superlattice which is not commonly seen in the heavy AM-GIC's. The micrograph is $\simeq 6$ Å^{-1} across. (b) Sketch of the in-plane unit cell of a $p(\sqrt{3}\times\sqrt{3})R30°$ superlattice. This unit cell results in an exceptionally high in-plane rubidium density. (c) A computer simulation of how an electron diffraction micrograph of $p(\sqrt{3}\times\sqrt{3})R30°$ superlattice will appear in the analytical STEM. One of the six first-order (100) graphite spots has been circled in the upper left corner of the micrograph. The scale and orientation are the same as those in (a).

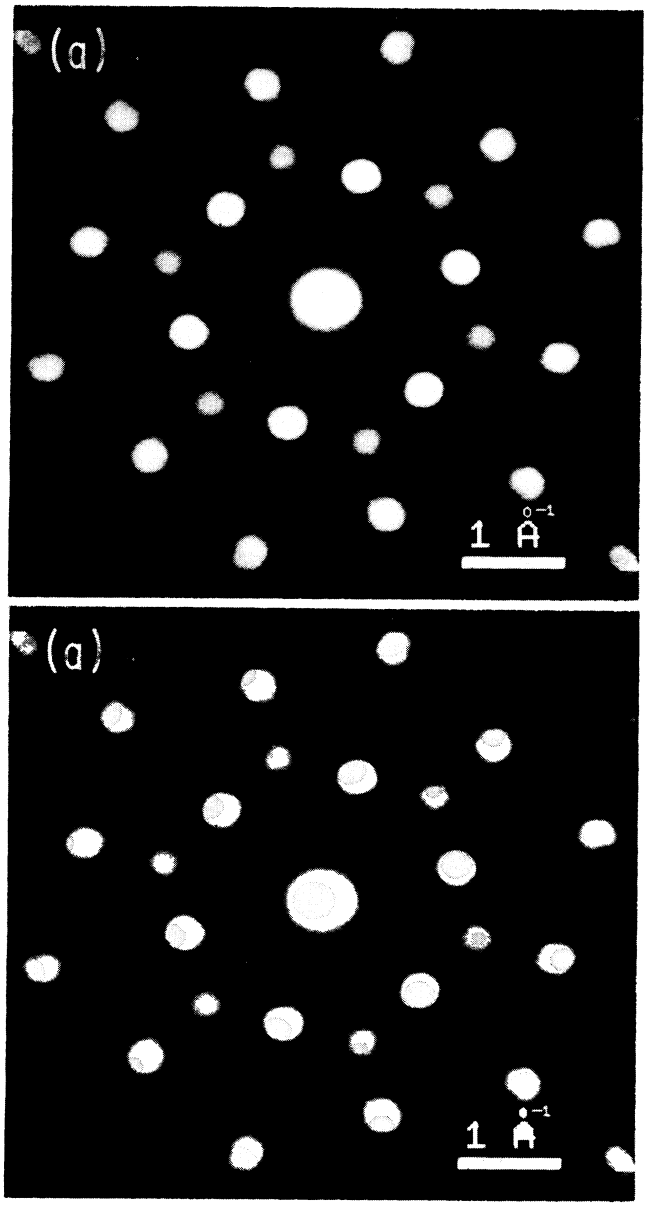

FIG. 5 (a) Diffraction micrograph of an area of the sample containing both a $p(2\times2)R0°$ and a $p(\sqrt{3}\times\sqrt{3})R30°$ superlattice at stage number two. The micrograph is $\simeq 6$ Å^{-1} across. (b) A computer simulation of how an electron diffraction micrograph of a combination of $p(2\times2)R0°$ and a $p(\sqrt{3}\times\sqrt{3})R30°$ superlattices will appear in the analytical STEM. One of the six first-order (100) graphite spots has been circled in the upper left corner of the micrograph. The scale and orientation are the same as those in (a).

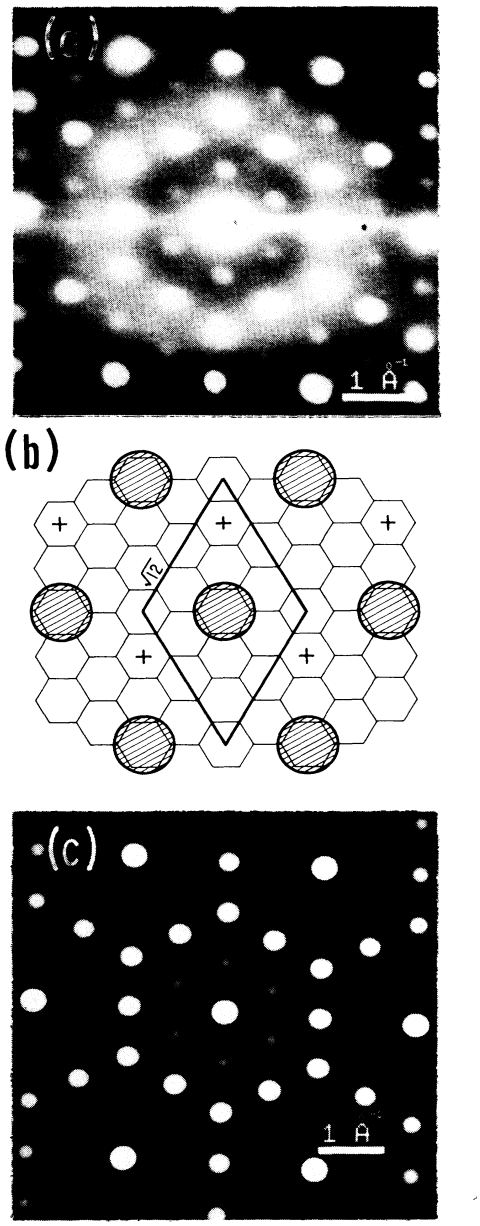

FIG. 6. (a) Diffraction micrograph showing a pattern which corresponds to an in-plane lattice $p(\sqrt{12}\times\sqrt{12})R30°$. This pattern appeared briefly and is probably a transition structure between stage-2 and stage-3. The micrograph is $\simeq 6$ Å^{-1} across. (b) Sketch of the in-plane unit cell of a $p(\sqrt{12}\times\sqrt{12})R30°$ superlattice. The + 's show the basis which would be necessary to create a "Rüdorff-like" structure, which is an $h(\sqrt{12}\times\sqrt{12})R30°$ superlattice. (c) A computer simulation of how an electron diffraction micrograph of a $p(\sqrt{12}\times\sqrt{12})R30°$ superlattice combined with the previous two lattices will appear in the analytical STEM. One of the six first-order (100) graphite spots has been circled in the upper left corner of the micrograph. The scale and orientation are the same as those in (a).

present while the $\sqrt{3}\times\sqrt{3}$ was still frequently present with varying intensity. In addition an amorphous ring again formed at 1.84 ± 0.1 Å^{-1} and grew in intensity throughout this time. We interpret this as an indication of a change in stage. During this time (about a week) three different "temporary" lattices were observed in

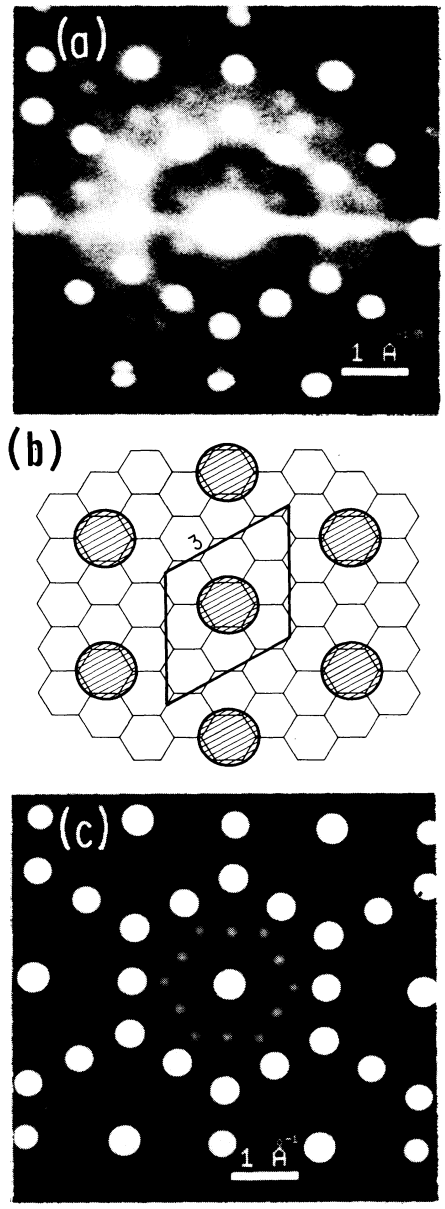

FIG. 7. (a) Diffraction micrograph of the sample while probably in a transition between stages, possibly from 3 to 4. This pattern is characteristic of a $p(3\times2)R0°$ superlattice which is not commonly seen in the heavy AM-GIC's. The micrograph is $\simeq 6$ Å^{-1} across. (b) Sketch of the in-plane unit cell of a $p(3\times3)R0°$ superlattice. (c) A computer simulation of how an electron diffraction micrograph of a $p(3\times3)R0°$ superlattice combined with the previous three lattices will appear in the analytical STEM. The scale and orientation are the same as those in (a).

various different and overlapping areas of the sample. The most widespread and intense of these was the previously seen $\sqrt{12}\times\sqrt{12}$ superlattice whose origin is probably the same as the first time it was observed. The second superlattice which was seen during this time was $p(3\times3)R0°$ and is also a commensurate hexagonal lattice. The diffraction pattern from this lattice is shown in Fig. 7(a). Figures 7(b) and 7(c) show the in-plane unit cell and resulting computer simulation for this lattice. Like the $\sqrt{12}\times\sqrt{12}$ lattice this lattice is easily produced by desorption from either a $\sqrt{3}\times\sqrt{3}$ or a 2×2 lattice.

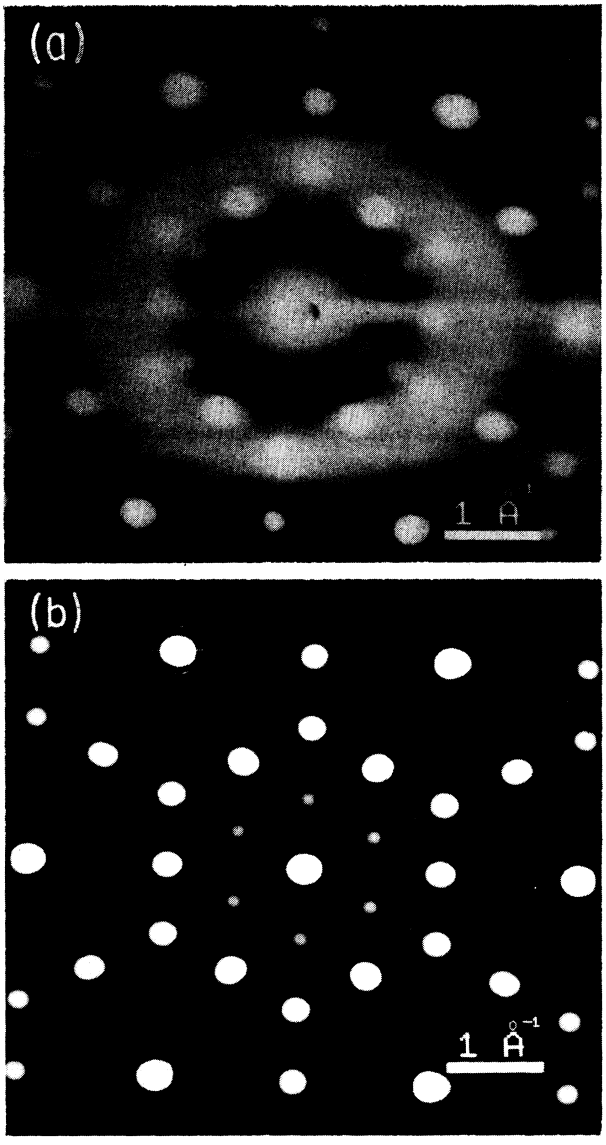

FIG. 8. (a) Diffraction micrograph of the sample while probably in a transition between stages, possibly from 3 to 4. This pattern is characteristic of two rotations of an incommensurate $r(4.6\times4.6$ Å) superlattice which is not commonly seen in the heavy AM-GIC's. The micrograph is $\simeq6$ Å^{-1} across. (b) A computer simulation of (a). One of the six first-order (100) graphite spots has been circled in the upper left corner of the micrograph.

The remaining temporary intercalant lattice produced first-order spots at 1.36 ± 0.05 Å^{-1} rotated 30° from the graphite inverse lattice. This lattice did not display hexagonal symmetry and this distance does not correspond

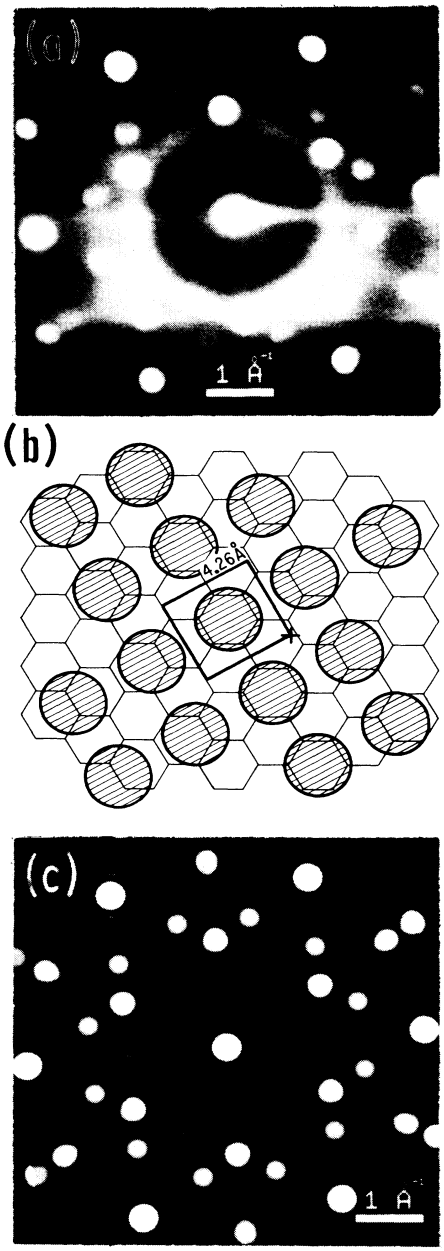

FIG. 9. (a) Diffraction micrograph of a stable incommensurate square lattice which is compatible with $r(4.26\times4.26$ Å) $R0°$ and a symmetric stacking sequence of two. (b) Sketch of the in-plane unit cell of an $r(4.26\times4.26$ Å) $R0°$ superlattice. The + 's show the location of the symmetric stacking order where the next intercalant plane would have to be located to reproduce the diffraction data. (c) A computer simulation of how an electron diffraction micrograph of $r(4.26\times4.26$ Å)$R0°$ combined with a $p(\sqrt{3}\times\sqrt{3})R30°$ superlattice and a disordered $p(2\times2)R0°$. One of the six first-order (100) graphite spots has been circled in the upper left corner of the micrograph. The scale and orientation are the same as those in (a).

to a commensurate graphite lattice or fit on the curve of Mori *et al.* It is compatible with a square-incommensurate lattice of size 4.6 ± 0.17 Å on a side with no rotation with respect to the graphite lattice. This structure can be interpreted as a nucleation of the next structure which seemed to characterize this stage. An electron diffraction pattern from this lattice is shown in Fig. 8(a) and a computer simulation in Fig. 8(b). The incommensurate spots in this figure can be generated either with two rotations of an $r(4.6\times4.6$ Å$)R0°$ lattice or with the same lattice with the rubidium ions registered into the nearest graphite center following the relaxed close-packed (rcp) model of DiCenzo.[31]

After the comparatively rapid structural changes ceased, the first long-term stable clearly incommensurate phase appeared. It coexisted with the previously seen $\sqrt{3}\times\sqrt{3}$ and weak 2×2 hexagonal lattices and coalesced from the disordered ring at 2.1 ± 0.1 Å^{-1}. The diffraction pattern from this structure had first-order spots at 2.086 ± 0.03 Å^{-1}, located $\pm15°$ ($\pm1°$) from the graphite inverse lattice vectors (for a total of 12). A diffraction micrograph containing this pattern is shown in Fig. 9(a). We have not been able to find a hexagonal lattice of any type which fits this diffraction pattern. This includes "normal" regular hexagonal lattices, rcp lattices, and lattices composed of registered sites in small domains. A $p(\sqrt{5}\times\sqrt{5})R0°$ superlattice is the smallest lattice which produces diffraction spots in the proper locations. The high degree of cancellation necessary for this lattice to reproduce our data rule a unit cell of this size out. We have found an incommensurate square lattice which fits the data. Three rotations of an $r(3.013\times3.013$ Å$)R\pm15°$ square lattice fits the data exactly. The interpretation of diffraction data from AM-GIC's in terms of nonhexagonal lattices is not new,[38] but incommensurate nonhexagonal lattices have not been previously suggested. The rubidium ion separation of only 3.01 ± 0.03 Å just barely allows this lattice to exist without any overlap of the ionic radii of rubidium ($r_{Rb^+}=1.47$ Å). This ionic separation is substantially less than that of crystalline rubidium (4.84 Å). A similar, less dense structure, which produces the same diffraction pattern, is a square $r(4.26\times4.26$ Å$)R0°$ with a two-layer intercalant correlation length and a symmetric stacking order. This lattice is shown in Fig. 9(b) along with the location of the necessary stacking position. The resulting computer simulation is shown in Fig. 9(c). This simulation was created by assuming a combination of a number of different lattices. Three rotations of the square lattice create the 12 incommensurate spots, a $\sqrt{3}\times\sqrt{3}$ lattice accounts for the commensurate spots and the weak lines are created by assuming a disordered 2×2 lattice. The intercalant nearest-neighbor distance of $\sqrt{3}$ times the graphite lattice or 4.26 Å results in a planar density for this structure which is greater than the maximum planar density of crystalline rubidium [(111) plane] but is consistent with the planar densities of structures which we observed earlier in this sample. If we assume that this structure has a third- or fourth-stage ordering, then the total density of the intercalant is 4.45×10^{-2} or 3.5×10^{-2} atoms/Å^3, which is 41% or 32% of that of pure rubidium, both of which seem reasonable.

Despite the fact that at this time the specimen was developing a succession of interesting structures and our equipment was providing more than enough signal to continue, the experiment had to be terminated due to a minor equipment failure which necessitated opening the high vacuum column to the ambient atmosphere.

SUMMARY

We see both cases of relative interaction strength. In the regime of high intercalant density the host-intercalant interactions dominate, forcing the intercalant into regular triangular arrays in registered lattice sites. At lower densities the rubidium is able to form high-planar-density materials whose periodicities are the result of the intercalant-intercalant interactions creating highly incommensurate lattices.

In addition to the unusual in-plane structures which were observed, this experiment is notable for what was not observed. As previously mentioned the majority of the previous work has reported three structural phase regimes below room temperature in the higher-stage heavy AM-GIC's. Our experiment covered this entire range without producing any signs of phase transitions. In the high-temperature regime we observed commensurate structures where previously only disordered liquid-like behavior had been observed. These structures persisted well into the low-temperature regime where previous observations have seen only incommensurate behavior.

The commensurate lattices which we observed were not the previously observed $p(\sqrt{7}\times\sqrt{7})R19.1°$ upon which the discommensurate domain model is based. Instead we saw a $p(2\times2)R0°$ lattice at much higher stage number than previously observed. At high stage number the sample also produced a $p(\sqrt{3}\times\sqrt{3})R30°$ structure which has a much higher two-dimensional density than the previously seen structures. Two commensurate transition structures were also observed along with an incommensurate transition structure.

A dense in-plane lattice does not necessarily imply an overall high in-plane intercalant density and may still be compatible with previous stoichiometric results. Most of the rubidium was nucleated into islandlike structures with gaps between these islands. The combination of alternating dense and diffuse areas could easily lead to an overall stoichiometry similar to that of earlier results.

The reasons for the discrepancies between previous results and our experiment are not clear. One set of possibilities involves our equipment. Our analytical STEM produces much higher beam densities than normally used which might disrupt the intercalant superlattice through heating or collision damage. An electron diffraction study involving a STEM has a much higher spatial resolution than other techniques. We operated with a resolution of a few hundreds of angstroms, which is at least a factor of 10 better than conventional TEM's can achieve and more than a factor of 100 better than x-ray diffraction methods. In addition our relatively low

beam energy of 26 kV limited this study to thin specimen areas which might not be as characteristic of a bulk sample as we would hope. A second factor which might contribute to the discrepancy involves the sample preparation and microdefect structure of the graphite host. The behavior of GIC's seems to vary widely even when being examined by similar techniques. This brings up the possibility that the detailed behavior of GIC's is strongly dependent on variables which are not easily controllable.

ACKNOWLEDGMENTS

I would like to thank N. Parker, M. Utlaut, W. Mankawich, E. Kritchman, and the University of Chicago Division of Physical Sciences, Central Shop for substantial efforts during the initial development phase of the microscope. I am grateful to Dr. D. M. Hwang of Bell Communication Research for providing me with the samples and valuable discussion. I wish to thank IBM for their cooperation in the use of the 4381 system, Metheus Corp. for the donation of the Metheus 500 image display and storage system, and Guy McNamara for his contribution to the imaging and analysis system. I would also like to thank Dr. A. V. Crewe for the use of his laboratory, his encouragement, and invaluable input into this project. Project funding was supplied under National Science Foundation Contract No. DMR8513954 and Department of Energy Contracts No. DEACO276EV02398 and No. DEFG0286ER60437. This paper has been presented as a thesis to the Department of Physics, The University of Chicago, in partial fulfillment of the requirements for the Ph.D. degree.

[1]For a more comprehensive review of GIC's see the following three references.
[2]S. A. Solin, Adv. Chem. Phys. **49**, 455 (1982).
[3]M. S. Dresselhaus and G. Dresselhaus, Adv. Phys. **30**, 139 (1981).
[4]H. Zabel and P. C. Chow, Comments Condensed Mat. Phys. **12**, 225 (1986).
[5]The Chinese cured clay through an intercalation process before using it for making porcelain pottery. A. Weiss, Ange. Chem. **2**, 697 (1963).
[6]P. Schaffäutl, J. Prakt. Chem. **21**, 155 (1841).
[7]U. Hoffmann and A. Frenzel, Z. Elektrochem. **37**, 613 (1931).
[8]A. Schleede and M. Wellmann, Z. Phys. Chem. **18**, 1 (1932).
[9]J. M. Thomas and G. R. Millward, Mater. Res. Bull. **15**, 671 (1980).
[10]W. D. Ellenson, D. Semmingsen, D. Guerard, D. G. Onn, and J. E. Fisher, Mater. Sci. Eng. **31**, 137 (1977).
[11]N. Daumas and A. Hérold, Bull. Soc. Chim. Fr. **5**, 1589 (1971).
[12]N. B. Hanny, T. H. Geballe, B. T. Matthias, K. Andres, P. Schmidt, and D. MacNair, Phys. Rev. Lett. **14**, 225 (1965).
[13]Y. Koike, H. Suematsu, K. Higuchi, and S. Tanuma, Solid State Commun. **27**, 623 (1978).
[14]N. Wada, Phys. Rev. B **24**, 1065 (1981).
[15]R. Clarke, N. Caswell, S. A. Solin, and P. M. Horn, Phys. Rev. Lett. **43**, 2018 (1979); R. Clarke, N. Caswell, S. A. Solin, and P. M. Horn, in Proceedings of the International Conference on Layered Materials and Intercalates, Nijmegen, The Netherlands, 1979 [Physica **99B**, 457 (1980); R. Clarke, N. Caswell, and S. A. Solin, Phys. Rev. Lett. **42**, 61 (1979).
[16]K. Fredenhagen and G. Cadenbach, Z. Anorg. Allg. Chem. **158**, 249 (1926).
[17]W. Rüdorff and E. Schulze, Z. Anorg. Chem. **277**, 156 (1954).
[18]Notation refers to a triangular lattice [*p* for close packed, *h* for honeycombed (hexagonal), *r* for rectangular, and *o* for oblique] with lattice vectors twice as long as the graphite lattice vectors (2×2.46 Å$=4.91$ Å), and rotated zero degrees from the graphite lattice.
[19]G. S. Parry and D. E. Nixon, Nature (London) **219**, 910 (1967); G. S. Parry, D. E. Nixon, K. M. Lester, and B. C. Levene, J. Phys. Chem. **2**, 2156 (1969).
[20]N. Kambe, G. Dresselhaus, and M. S. Dresselhaus, Phys. Rev. B **21**, 3491 (1980).
[21]N. Caswell, Phys. Rev. B **22**, 6308 (1980).
[22]H. Suematsu, M. Suzuki, H. Ikeda, and S. Tanuma, Sci. Rep. Res. Tohoku Univ., Ser. A **27**, Suppl. 1, 97 (1979).
[23]D. D. L. Chung, G. Dresselhaus, and M. S. Dresselhaus, Mater. Sci. Eng. **31**, 107 (1977).
[24]F. Rousseaux, R. Moret, D. Guerard P. Lagrange, and M. Lelaura, Synth. Met. **12**, 45 (1985).
[25]M. Suzuki, H. Ikeda, H. Suematsu, Y. Endoh, H. Shiba, and M. T. Hutchings, J. Phys. Soc. Jpn. **49**, 671 (1980).
[26]H. Zabel, C. S. Moss, N. Caswell, and S. A. Solin, Phys. Rev. Lett. **43**, 2022 (1979).
[27]M. Mori, S. C. Moss, Y. M. Jan, and H. Zabel, Phys. Rev. B **25**, 1287 (1982).
[28]N. Caswell, S. A. Solin, T. M. Hayes, and S. J. Hunter, Physica **99B**, 463 (1980).
[29]R. Clarke, J. N. Gray, H. Homma, and M. J. Winokur, Phys. Rev. Lett. **47**, 1407 (1981).
[30]F. C. Frank and J. H. ven der Merwe, Proc. R. Soc. London, Ser. A **198**, 205 (1949); **198**, 216 (1949).
[31]S. B. DiCenzo, Phys. Rev. B **26**, 5878 (1982).
[32]D. M. Hwang, X. W. Qian, and S. A. Solin, Phys. Rev. Lett. **53**, 1473 (1984).
[33]D. M. Hwang and G. Nicolaides, Solid State Commun. **49**, 483 (1984).
[34]N. W. Parker, R. K. Mittleman, and A. V. Crewe, Rev. Sci. Instrum. **58**, 174 (1987).
[35]G. R. McNamara. O. H. Kapp, and A. V. Crewe, in Proceedings of the 13th International Congress of Biochemistry, Amsterdam, 1985 (unpublished), p. 155.
[36]Multiple scattering from the graphite is not a factor (it merely changes the graphite spot intensities) and except for the stage-1 material there is not enough rubidium present to observe multiple scattering.
[37]A. Mansour, S. E. Schnatterly, and J. J. Ritsko, Phys. Rev. Lett. **58**, 614 (1987).
[38]D. M. Hwang, N. W. Parker, M. Utlaut, and A. V. Crewe, Phys. Rev. Lett. **27**, 1458 (1983).

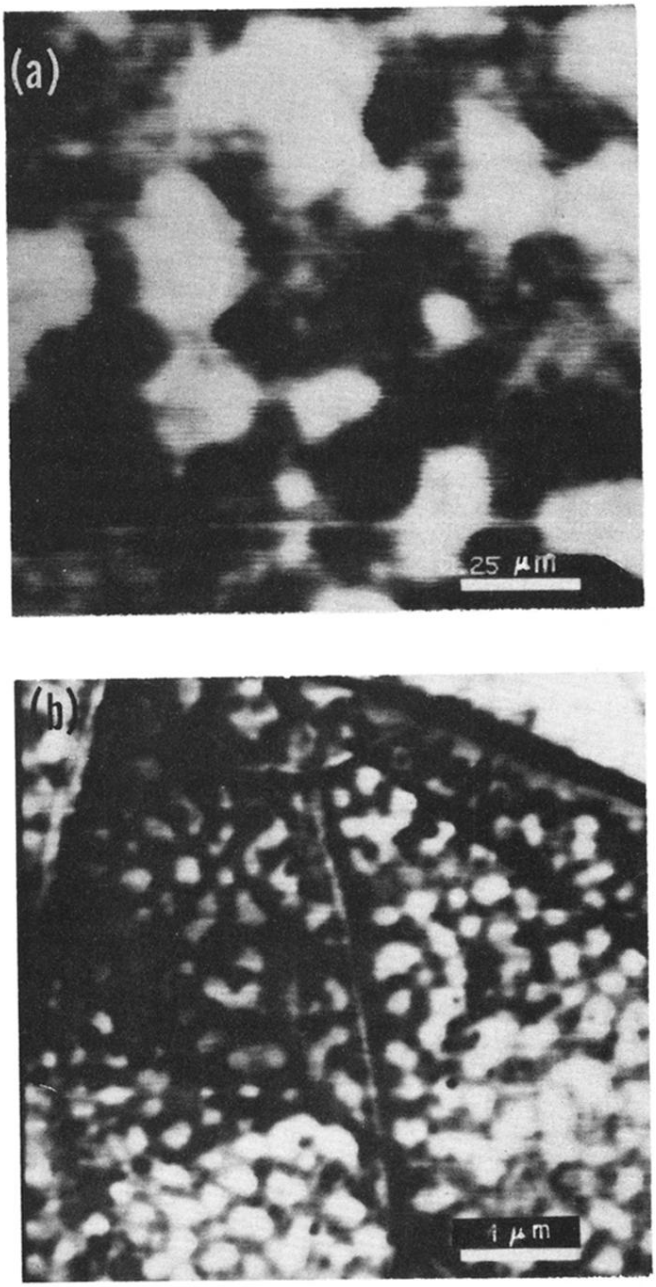

FIG. 1. Dark-field STEM image taken using the elastically scattered electrons. (a) The full scale of the image is 1.4 μm and demonstrates the presence of small islands of rubidium formed within the graphite host. (b) The full scale of the image is 5.6 μm. The dark lines are the boundaries of the HOPG domains.

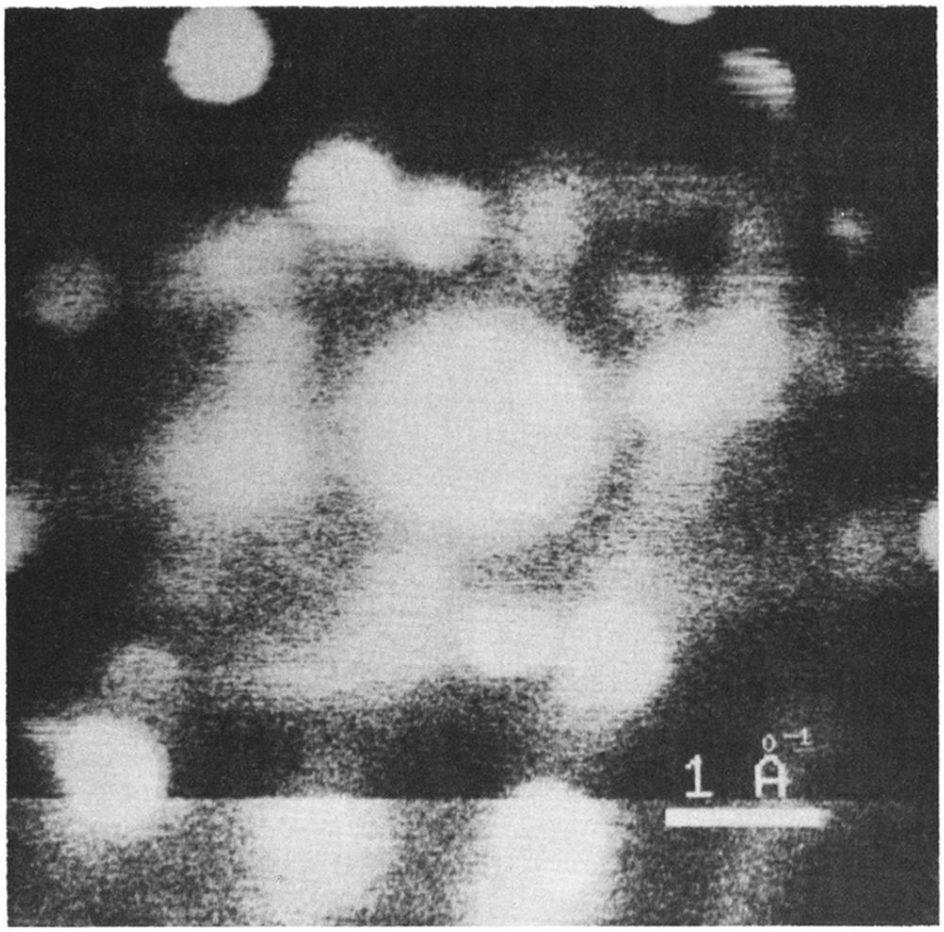

FIG. 2. Diffraction micrograph of a saturated rubidium intercalated graphite immediately after insertion into the analytical STEM. It shows two rotations of a disordered $2\times\sqrt{3}$ superlattice. The graphite diffraction is difficult to see due to the large amount of obscuring rubidium scattering. The micrograph is $\simeq 6$ Å^{-1} across.

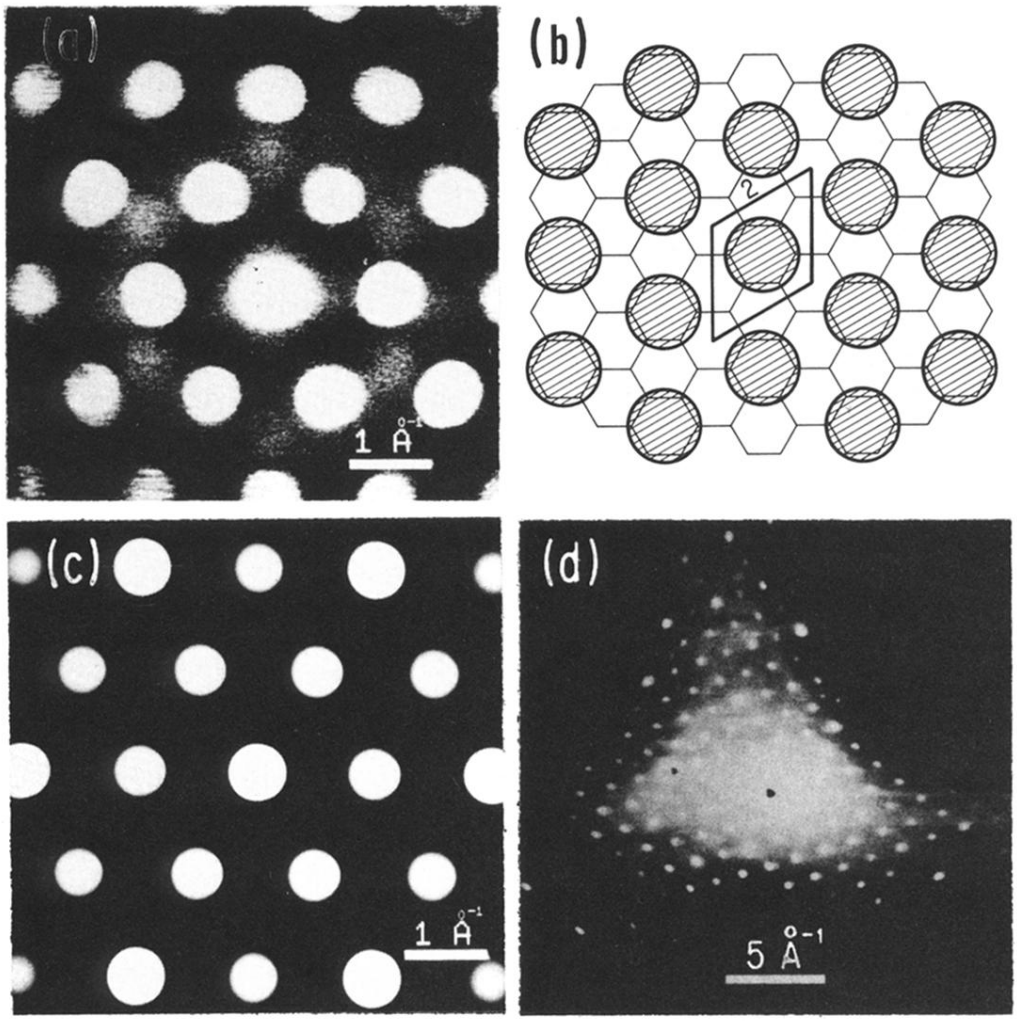

Fig. 3. (a) Diffraction micrograph of the sample while at stage 1. This pattern is characteristic of the $p(2\times2)R0°$ superlattice which is commonly seen in stage-1 heavy AM-GIC's. The micrograph is $\simeq 6$ Å^{-1} across. (b) Sketch of the in-plane unit cell of $p(2\times2)R0°$. The circles represent the locations of the rubidium ions, which are drawn to scale ($r_{Rb^+} = 1.47$ Å). (c) A computer simulation of how an electron diffraction micrograph of $p(2\times2)R0°$ will appear in the analytical STEM. One of the six first-order (100) graphite spots (2.95 Å^{-1}) has been circled in the upper left corner of the micrograph. The scale and orientation are the same as those in (a). (d) Lower-magnification diffraction micrograph of $p(2\times2)R0°$ superlattice. Diffraction from this superlattice is visible beyond 14 Å^{-1}.

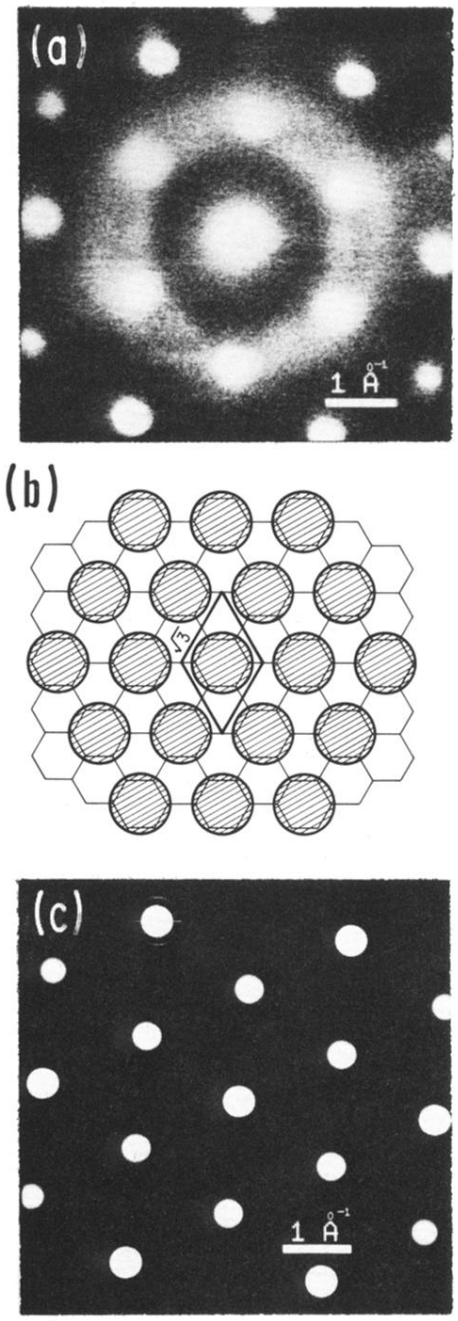

FIG. 4. (a) Diffraction micrograph of the sample while probably at stage number two. This pattern is characteristic of a $p(\sqrt{3}\times\sqrt{3})R30°$ superlattice which is not commonly seen in the heavy AM-GIC's. The micrograph is $\simeq 6$ Å^{-1} across. (b) Sketch of the in-plane unit cell of a $p(\sqrt{3}\times\sqrt{3})R30°$ superlattice. This unit cell results in an exceptionally high in-plane rubidium density. (c) A computer simulation of how an electron diffraction micrograph of $p(\sqrt{3}\times\sqrt{3})R30°$ superlattice will appear in the analytical STEM. One of the six first-order (100) graphite spots has been circled in the upper left corner of the micrograph. The scale and orientation are the same as those in (a).

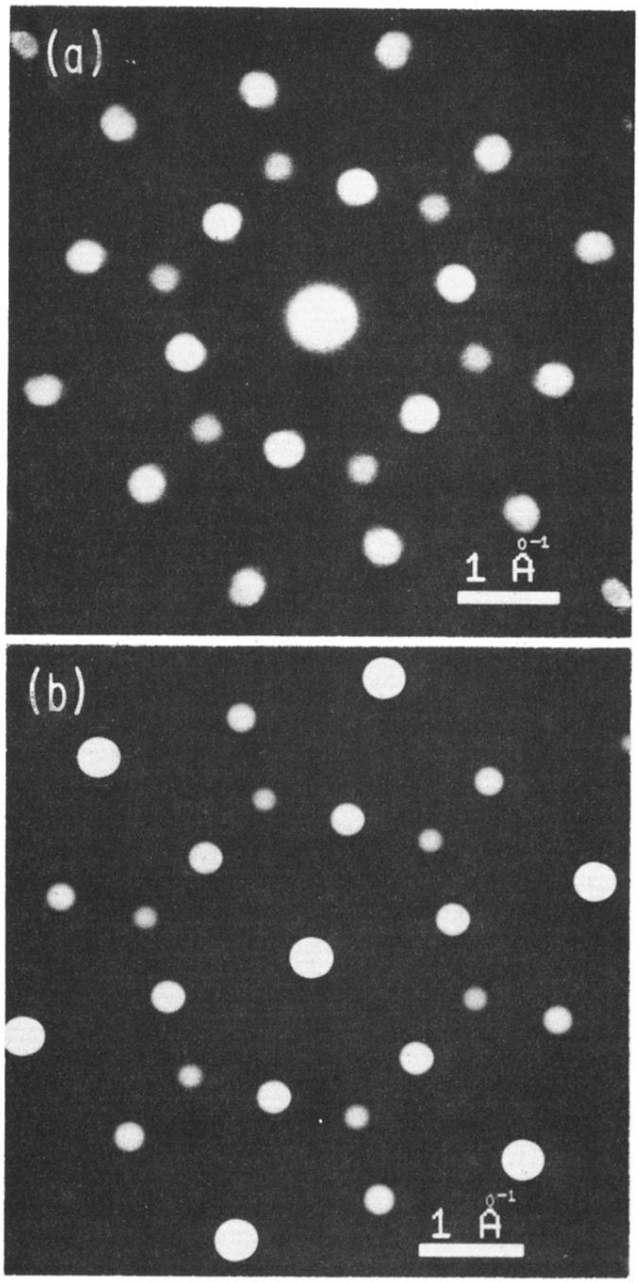

FIG. 5 (a) Diffraction micrograph of an area of the sample containing both a $p(2\times2)R0°$ and a $p(\sqrt{3}\times\sqrt{3})R30°$ superlattice at stage number two. The micrograph is $\simeq 6$ Å^{-1} across. (b) A computer simulation of how an electron diffraction micrograph of a combination of $p(2\times2)R0°$ and a $p(\sqrt{3}\times\sqrt{3})R30°$ superlattices will appear in the analytical STEM. One of the six first-order (100) graphite spots has been circled in the upper left corner of the micrograph. The scale and orientation are the same as those in (a).

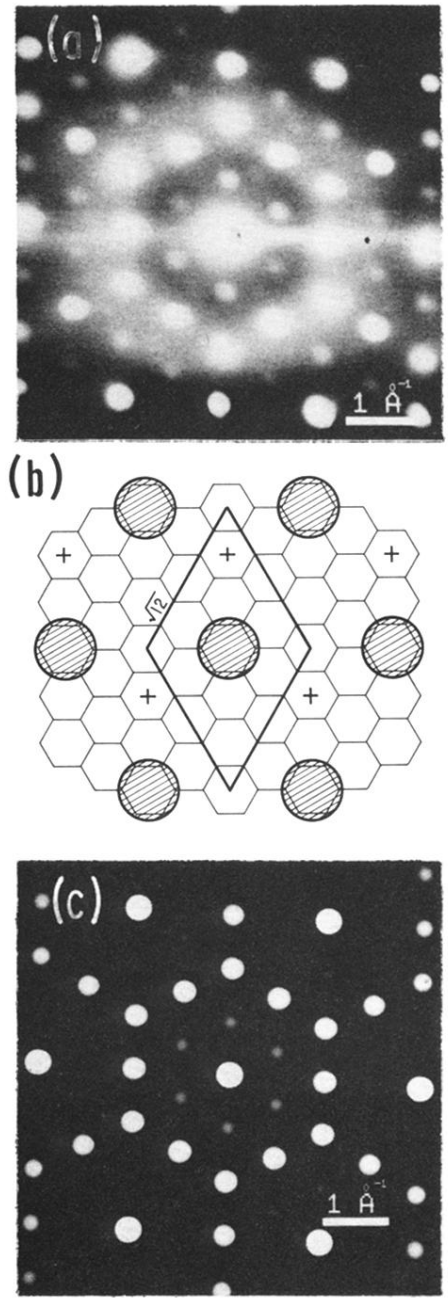

FIG. 6. (a) Diffraction micrograph showing a pattern which corresponds to an in-plane lattice $p(\sqrt{12}\times\sqrt{12})R30°$. This pattern appeared briefly and is probably a transition structure between stage-2 and stage-3. The micrograph is $\simeq 6$ Å^{-1} across. (b) Sketch of the in-plane unit cell of a $p(\sqrt{12}\times\sqrt{12})R30°$ superlattice. The $+$'s show the basis which would be necessary to create a "Rüdorff-like" structure, which is an $h(\sqrt{12}\times\sqrt{12})R30°$ superlattice. (c) A computer simulation of how an electron diffraction micrograph of a $p(\sqrt{12}\times\sqrt{12})R30°$ superlattice combined with the previous two lattices will appear in the analytical STEM. One of the six first-order (100) graphite spots has been circled in the upper left corner of the micrograph. The scale and orientation are the same as those in (a).

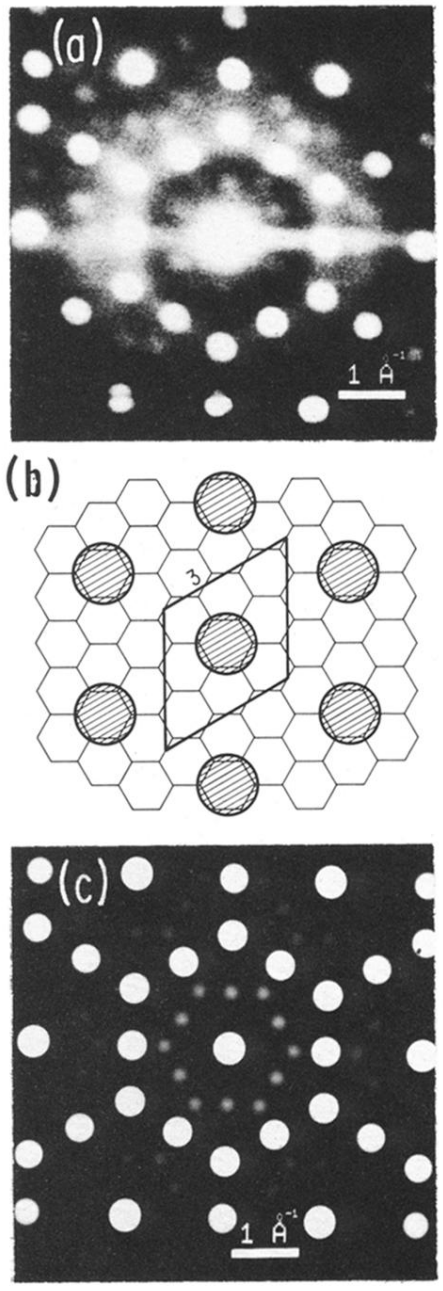

FIG. 7. (a) Diffraction micrograph of the sample while probably in a transition between stages, possibly from 3 to 4. This pattern is characteristic of a $p(3\times2)R0°$ superlattice which is not commonly seen in the heavy AM-GIC's. The micrograph is $\simeq 6$ Å^{-1} across. (b) Sketch of the in-plane unit cell of a $p(3\times3)R0°$ superlattice. (c) A computer simulation of how an electron diffraction micrograph of a $p(3\times3)R0°$ superlattice combined with the previous three lattices will appear in the analytical STEM. The scale and orientation are the same as those in (a).

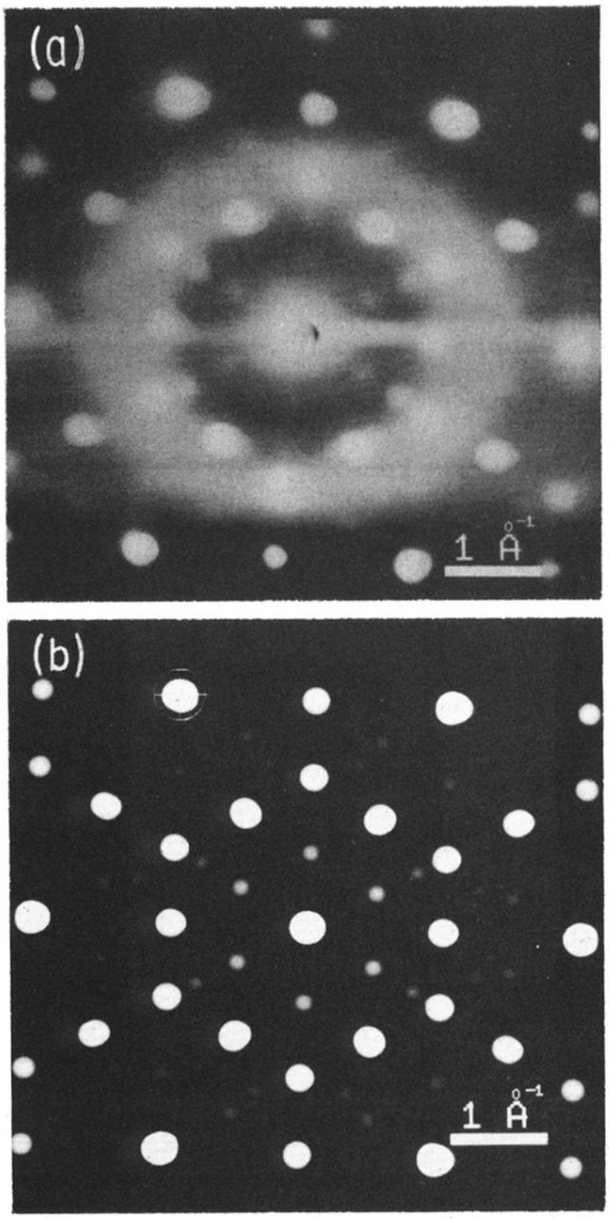

FIG. 8. (a) Diffraction micrograph of the sample while probably in a transition between stages, possibly from 3 to 4. This pattern is characteristic of two rotations of an incommensurate $r(4.6\times4.6$ Å) superlattice which is not commonly seen in the heavy AM-GIC's. The micrograph is $\simeq 6$ Å^{-1} across. (b) A computer simulation of (a). One of the six first-order (100) graphite spots has been circled in the upper left corner of the micrograph.

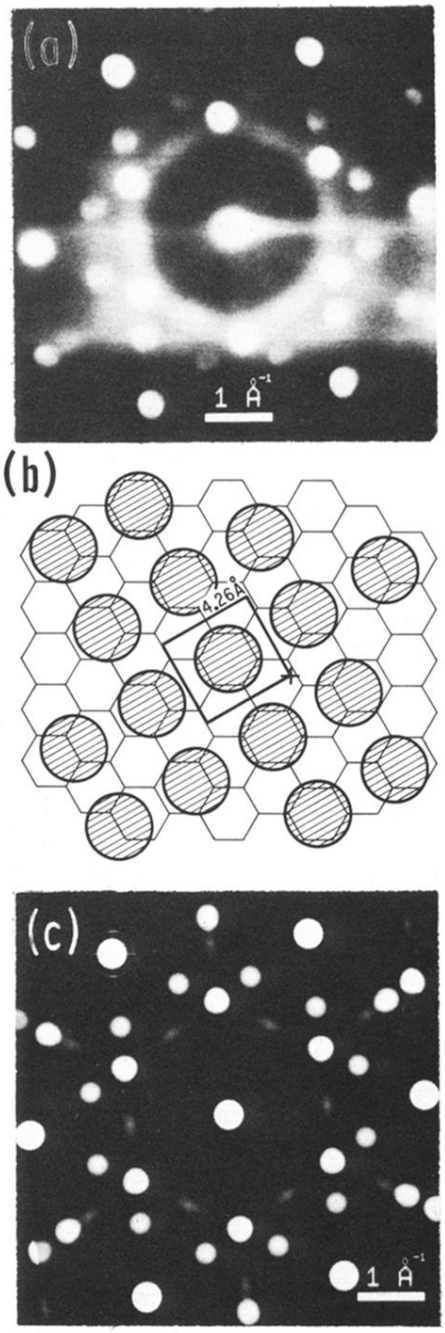

FIG. 9. (a) Diffraction micrograph of a stable incommensurate square lattice which is compatible with $r(4.26\times4.26$ Å$)$ $R0°$ and a symmetric stacking sequence of two. (b) Sketch of the in-plane unit cell of an $r(4.26\times4.26$ Å$)$ $R0°$ superlattice. The $+$'s show the location of the symmetric stacking order where the next intercalant plane would have to be located to reproduce the diffraction data. (c) A computer simulation of how an electron diffraction micrograph of $r(4.26\times4.26$ Å$)R0°$ combined with a $p(\sqrt{3}\times\sqrt{3})R30°$ superlattice and a disordered $p(2\times2)R0°$. One of the six first-order (100) graphite spots has been circled in the upper left corner of the micrograph. The scale and orientation are the same as those in (a).